NUMERICAL SIMULATION OF DROPLET-DEFORMATION BY A LEVEL SET APPROACH WITH SURFACE TENSION

ROBERTO CROCE*, MICHAEL GRIEBEL*, MARC ALEXANDER SCHWEITZER*

Abstract. In this paper we present a three-dimensional Navier–Stokes solver for incompressible two-phase flow problems with surface tension and apply the proposed scheme to the simulation of droplet-deformation. Our approach employs a standard finite difference/finite volume discretization on uniform Cartesian staggered grids and uses Chorin's projection approach. The free surface between the two fluid phases is tracked with a level set technique. Here, the interface conditions are implicitly incorporated into the momentum equations by the continuum surface force method. Surface tension is evaluated using a smoothed delta function and third order interpolation. The problem of mass conservation for the two phases is treated by a reinitialization of the level set function employing a regularized signum function and a global fixed point iteration. All convective terms are discretized by a WENO scheme of fifth order. Altogether, our approach exhibits a second order convergence away from the free surface. The discretization of surface tension requires a smoothing scheme near the free surface which leads to a first order convergence in the smoothing region.

We discuss the details of the proposed numerical scheme and present the results of several numerical experiments concerning mass conservation, convergence of curvature and the application of our solver to the simulation of droplet-deformation due to a shear flow in three space dimensions.

Key words. incompressible two-phase flow, surface tension, capillarity, continuum surface force method, level set method, droplet

AMS subject classifications. 76B45, 76T10, 76M20

1. Introduction. Many problems in fluid flow applications require the consideration of two incompressible immiscible fluids and, consequently, the treatment of the free surface between these two phases. Important examples are the deformation of liquid-gas interfaces by aerodynamical forces as it occurs in spray injection and atomization in liquid propulsion [32]. A reference problem in dispersion science, emulsification and mixing is the deformation of a liquid droplet due to a surrounding shear flow. In such mesoscopic flow problems, when the characteristic length scale of the flow is relatively small, surface tension effects cannot be neglected as in (most) macroscopic flows. The forces due to surface tension play an essential role for the overall dynamics and determine the deformation behavior of the interface. This class of applications pose a number of challenges to numerical methods. The most substantial is the representation of the moving interface which separates the two different fluid phases and their associated material properties like density and viscosity, and the appropriate treatment of surface tension effects.

Classical approaches to the tracking of moving interfaces are the Marker and Cell (MAC) schemes [2, 11, 12, 20, 22, 24, 36, 46, 47] where the two fluid phase are explicitly represented by massless marker particles and the interface needs to be reconstructed from the distribution of the marker particles. The accurate representation of the moving interface however requires a large number of marker particles and thereby a substantial computational effort. In the Volume of Fluid (VOF) technique [4, 13, 23, 25, 30, 33, 34, 37] the characteristic functions of the two fluid domains are directly approximated on the underlying mesh by a piecewise constant function. Hence, the reconstruction of a smooth interface, i.e., the accurate computation of curvature which is necessary for simulations involving surface tension effects, is not straightforward

*Institut für Numerische Simulation, Universität Bonn, Wegelerstr. 6, D-53115 Bonn, Germany (croce@ins.uni-bonn.de, griebel@ins.uni-bonn.de, schweitzer@ins.uni-bonn.de).

in VOF and requires sophisticated interpolation schemes [18, 19]. This drawback is overcome in the level set (LS) approach [38, 39, 42] where the characteristic functions of the two fluid phases are approximated by the sign of a smooth scalar function, so that the interface is given by the zero-level set of this smooth function. Due to this smooth approximation the computation of curvature is straightforward.

The movement of the interface, however, may lead to a substantial distortion of the level set function over time; i.e., its gradient may become very large or very small near the interface which can adversely effect the stable evaluation of surface tension terms. To overcome this issue a so-called reinitialization step must be performed. Here, the current level set function is replaced by a smoother, less distorted function which has (approximately) the same zero-level set. This however may compromise the mass conservation properties of the numerical scheme. A widely used and very successful approach is the reinitialization by a signed distance function, see e.g. [1, 7, 8, 35, 45]. Such a simple reinitialization technique, however, introduces numerical diffusion to the solution which leads to a deterioration of the volume conservation, i.e. mass conservation in incompressible flow. To this end, several modified reinitialization methods have been developed to improve mass conservation [17, 40, 41, 44]. However, the interplay between these techniques and the convergence behavior of surface tension terms within a full two-phase flow solver is not completely understood.

The second major challenge encountered in the simulation of multi-phase flows on the mesoscale is the numerical treatment of surface tension effects which cannot be neglected. One approach to the treatment of surface tension is by variational techniques based on the Laplace–Beltrami operator on the free surface [3, 14, 15, 26, 27]. Another widely used approach is the Continuum Surface Force (CSF) scheme [5, 47]. Here, surface tension, i.e., the respective interface condition, is modeled as a body force acting on grid cells that contain the interface. This approach was introduced in the context of VOF and MAC methods but it is directly applicable to the level set approach as well [45]. Even though, the CSF approach is reported to be quite robust, to our knowledge, the convergence behavior of surface tension terms approximated by the CSF in conjunction with a level set method within a full two-phase flow solver is also not completely understood.

In this paper we present a fully three-dimensional incompressible Navier–Stokes solver for two-phase flow problems based on Chorin's projection approach on staggered Cartesian grids, the level set technique and the CSF scheme for the treatment of surface tension effects. To cope with the issue of mass conservation we employ an improved reinitialization scheme essentially due to [45] in conjunction with a fifth order WENO scheme and an additional fixed point iteration to enforce the conservation of the global mass explicitly. We apply our solver to simulate the deformation of a droplet in three dimensions due to a shear flow.

The remainder of this paper is organized as follows: The employed mathematical model is presented in section 2. Here, we implement the coupling of the Navier–Stokes equations for two flow phases by classical interface conditions which incorporate surface tension. To this end, we discuss the CSF method in the context of the level set method (LSM). The discretization of the coupled model is presented in some detail in section 3. The Navier–Stokes equations as well as the transport equation for the level set function are discretized in time using an Adams–Bashford method of second order, whereas the reinitialization of the level set function is discretized in time using an explicit third order Runge–Kutta scheme. The discretization in space employs a standard finite difference / finite volume approach on a staggered uniform

2

grid. Furthermore, we use a signed distance function in the level set representation of the free surface, a fifth order WENO scheme for all convective terms, a higher order interpolation scheme for the level set function, and an improved reinitialization scheme including a global fixed point iteration to enforce mass conservation. In section 4 we present the results of several numerical experiments for model problems concerning mass conservation, convergence of curvature and convergence of the complete two-phase flow scheme. Finally, we consider the deformation of a liquid droplet due to a surrounding shear flow. We conclude with some remarks in section 5.

2. Mathematical Model. The behavior of two immiscible incompressible fluids is governed by the incompressible Navier–Stokes equations defined on an open set $\Omega = \Omega_1 \cup \Omega_2 \cup \Gamma_f \subset \mathbb{R}^3$ with Lipschitz boundary $\Gamma := \partial\Omega$. Here Ω_1 and Ω_2 denote the subdomains associated with the two different fluid phases, respectively. The free interface between the two fluid phases is denoted by $\Gamma_f := \partial\Omega_1 \cap \partial\Omega_2$. The two fluid domains Ω_1 and Ω_2, and the free interface Γ_f depend on time. The temporal evolution of each of the fluids is described by the classical Navier–Stokes equations in its respective subdomain Ω_i for $t \in [0, T]$; i.e., we have

$$
\begin{aligned}
\rho_i \frac{D\vec{u}_i}{Dt} &= -\nabla p_i + \nabla \cdot (\mu_i \mathbf{S}_i) + \rho_i \vec{g} & \text{in } \Omega_i, \\
\nabla \cdot \vec{u}_i &= 0 & \text{in } \Omega_i, \\
\vec{u}_i|_\Gamma &= 0 & \text{in } [0,\text{T}] , \\
\vec{u}_i|_{t=0} &= u_{0_i} & \text{in } \Omega_i,
\end{aligned}
\tag{2.1}
$$

where $i \in \{1, 2\}$ indicates the considered fluid phase. Furthermore, $\vec{u}_i$ denotes the velocity-field, p_i the pressure, μ_i the dynamic viscosity, ρ_i the density, and $\vec{g}$ the volume force. The viscous stress tensor is given by $\mathbf{S}_i := \nabla\vec{u}_i + \{\nabla\vec{u}_i\}^T$ and the material derivative by $\frac{D(\vec{u}_i)}{Dt} := \partial_t(\vec{u}_i) + (\vec{u}_i \cdot \nabla)\vec{u}_i$. The values of μ_i and ρ_i in each phase are assumed to be constant. However, the system (2.1) is *not* complete without some additional conditions imposed on the free interface Γ_f.

The basic assumption in continuum mechanics for the free boundary Γ_f is that it can be regarded as a sharp interface; i.e., the interface is a two-dimensional surface which separates the two flow regions. For immiscible fluids this can be justified by dimension analysis, see [31] for a detailed discussion. Hence, our two-phase flow model contains a jump in density and a jump in viscosity across the free surface. A consequence of this assumption is that the interface possesses no mass. Consequently, the net stress vanishes along the interface. Furthermore, the velocity must be continuous across the free surface, i.e., $\vec{u}_1 = \vec{u}_2$ on Γ_f. For a more detailed discussion see [31]. The surface tension boundary conditions at the interface Γ_f between the two fluid phases are given by

$$
(\mathbf{T}_1 - \mathbf{T}_2) \cdot \vec{n} = \sigma\kappa\vec{n}, \qquad (\mathbf{T}_1 - \mathbf{T}_2) \cdot \vec{t} = \frac{\partial\sigma}{\partial\vec{t}}, \qquad \text{and} \qquad (\mathbf{T}_1 - \mathbf{T}_2) \cdot \vec{s} = \frac{\partial\sigma}{\partial\vec{s}},
$$

where $\mathbf{T}_i := -p_i\mathbf{I} + \mu_i\mathbf{S}_i$ denotes the stress tensor, σ is the surface tension coefficient determined by the physical properties of the considered fluids, and $\vec{n} := \vec{n}_1 = -\vec{n}_2$ denotes the surface normal on Γ_f, i.e., the outer normal on $\partial\Omega_1$. The local curvature κ is given by

$$
\kappa = \frac{1}{R_t} + \frac{1}{R_s}
\tag{2.2}
$$

with the radii R_t and R_s of curvature along coordinates t and s as shown in Figure 2.1. Since we assume that the material properties μ_i and ρ_i are constant in each Ω_i, the
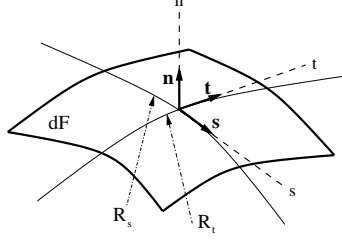
FIGURE 2.1. *Curvature for surface tension computation.*

surface tension coefficient σ is constant throughout the *whole* domain Ω. Therefore, the conditions on the interface Γ_f reduce to

$$\vec{u}_1 = \vec{u}_2, \tag{2.3}$$

$$(\mathbf{T}_1 - \mathbf{T}_2) \cdot \vec{n} = \sigma \kappa \vec{n}, \tag{2.4}$$

$$(\mathbf{T}_1 - \mathbf{T}_2) \cdot \vec{t} = 0, \tag{2.5}$$

$$(\mathbf{T}_1 - \mathbf{T}_2) \cdot \vec{s} = 0. \tag{2.6}$$

Throughout this paper, we consider surface tension forces in normal direction only. Hence, we complete the Navier–Stokes equations (2.1) in each of the subdomains Ω_i with the interface conditions (2.3) and (2.4) whereas the tangential conditions (2.5) and (2.6) are not explicitly enforced. Altogether, the complete model for two-phase flow problems including surface tension considered in this paper is given by

$$
\begin{array}{rcll}
\rho_i \dfrac{D\vec{u}_i}{Dt} &=& -\nabla p_i + \nabla \cdot (\mu_i \mathbf{S}_i) + \rho_i \vec{g} & \text{in } \Omega_i, \\[2mm]
\nabla \cdot \vec{u}_i &=& 0 & \text{in } \Omega_i, \\[1mm]
\vec{u}_i|_\Gamma &=& 0 & \text{in } [0,\text{T}] , \\[1mm]
\vec{u}_i|_{t=0} &=& u_{0_i} & \text{in } \Omega_i \\[1mm]
\vec{u}_1 &=& \vec{u}_2 & \text{on } \Gamma_f, \\[1mm]
(\mathbf{T}_1 - \mathbf{T}_2) \cdot \vec{n} &=& \sigma \kappa \vec{n} & \text{on } \Gamma_f,
\end{array}
\tag{2.7}
$$

for $i \in \{1, 2\}$.

2.1. Formulation of Surface Tension within the Momentum Equations.
To couple the two-phase-flow Navier–Stokes equations (2.1) with the free surface boundary conditions (2.4), we start from the integral form of (2.1)

$$\int_{\Omega_i} \rho_i \frac{D(\vec{u}_i)}{Dt} \, d\vec{x} = \int_{\partial\Omega_i} \mathbf{T}_i \cdot \vec{n} \, dF + \int_{\Omega_i} \rho_i \vec{g} \, d\vec{x} \tag{2.8}$$

for $i \in \{1, 2\}$. Summation of both momentum equations (2.8) yields

$$
\begin{aligned}
\rho_1 \int_{\Omega_1} &\frac{D\vec{u}}{Dt} d\vec{x} + \rho_2 \int_{\Omega_2} \frac{D\vec{u}}{Dt} \, d\vec{x} = \\
&\int_{\partial\Omega} \mathbf{T} \cdot \vec{n} \, dF - \int_{\Gamma_f} [\mathbf{T}] \cdot \vec{n} \, dF + \rho_1 \int_{\Omega_1} \vec{g} \, d\vec{x} + \rho_2 \int_{\Omega_2} \vec{g} \, d\vec{x}
\end{aligned}
\tag{2.9}
$$

where $\mathbf{T} := \mathbf{T}_1 \chi_{\Omega_1} + \mathbf{T}_2 \chi_{\Omega_2}$ is defined with the help of the characteristic functions χ_{Ω_1} and χ_{Ω_2} associated with the fluid domains Ω_1 and Ω_2 respectively. Furthermore,

4

$[\mathbf{T}]$ denotes the jump in the stress tensor T, i.e., $[\mathbf{T}] = \mathbf{T}_1 - \mathbf{T}_2$, at the interface Γ_f. With (2.4) and the Gauß Theorem, we obtain

$$\int_{\partial\Omega} \mathbf{T} \cdot \vec{n} \, dF = \int_{\Omega} \nabla \cdot \mathbf{T} \, d\vec{x}. \tag{2.10}$$

Since $\mathbf{T}$ is discontinuous at the free surface due to the jump in the viscosity, relation (2.10) is to be understood in the sense of distributions.

With (2.3), the velocity-field $\vec{u} = \vec{u}_1 \chi_{\Omega_1} + \vec{u}_2 \chi_{\Omega_2}$ for viscous fluids is continuous on Ω and we can write

$$\rho_1 \int_{\Omega_1} \frac{D\vec{u}}{Dt} \, d\vec{x} + \rho_2 \int_{\Omega_2} \frac{D\vec{u}}{Dt} \, d\vec{x} = \int_{\Omega} \rho \frac{D\vec{u}}{Dt} \, d\vec{x}. \tag{2.11}$$

Now we substitute (2.10) and (2.11) into (2.9) and obtain the integral formulation of incompressible two-phase flow with surface tension

$$\int_{\Omega} \rho \frac{D\vec{u}}{Dt} \, d\vec{x} = \int_{\Omega} \nabla \cdot \mathbf{T} \, d\vec{x} - \int_{\Gamma_f} \sigma \kappa \vec{n} \, dF + \int_{\Omega} \rho \vec{g} \, d\vec{x}. \tag{2.12}$$

The advantage of (2.12) is that the boundary condition for surface tension is implicitly contained in the momentum equation. However, it is still formulated as a free boundary integral. For the discretization we convert this free boundary integral to a volume integral via the CSF approach [5, 47]. Then, we can easily couple the momentum equation with a level set formulation which does not require an explicit reconstruction of the free surface. Note that this is in contrast to VOF methods where a reconstruction of Γ_f is required even with a CSF formulation.

2.2. The CSF-approach in the LSM. The CSF model was first proposed by Brackbill et al. [5] for VOF methods and by Unverdi et al. [47] for MAC methods. We now give a short description of the CSF approach in the framework of the level set method, see [45] for details.

The aim is to provide a unified formulation of (2.7) on the compete domain Ω; i.e., we will eliminate the explicit interface conditions in (2.7). To this end, we start from the two-phase flow equations in integral form (2.12). There, surface tension is included as a source-term on the right-hand side. Since our discretization will be based on the differential expression of the Navier–Stokes equations, this free boundary integral needs to be converted into a volume integral and, by passing to the limit of infinitesimally small volumes, we then obtain the associated differential expression of the Navier–Stokes equations.

To this end, we construct a function ϕ such that the interface between the two different fluids is the zero level set of ϕ, compare Figure 2.2. The interface is then given by

$$\Gamma_f(t) = \{\vec{x} : \phi(\vec{x}, t) = 0\}$$

for all times $t \in [0, T]$. Note that there are arbitrarily many ways to define the level set function ϕ away from the free surface. Here, we choose ϕ as a signed distance function such that

$$\phi(\vec{x}, t) \begin{cases} < 0 & \text{if } \vec{x} \in \Omega_1 \\ = 0 & \text{if } \vec{x} \in \Gamma_f \\ > 0 & \text{if } \vec{x} \in \Omega_2 \end{cases} \tag{2.13}$$
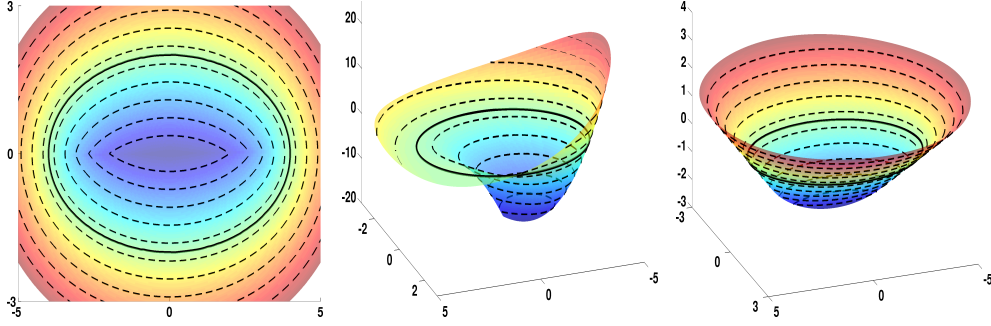
FIGURE 2.2. *Elliptical zero-level set (left; bold line, top view), surface plot of a general level set function with the same elliptical zero-level set (center), and a surface plot of a respective signed-distance level set function (right).*

hold and the Eikonal equation $|\nabla\phi| = 1$ is fulfilled, compare Figure 2.2. With the help of this level set function ϕ we can now easily define the density ρ and the viscosity μ on the whole domain, i.e., of both fluid-phases. To this end, we set

$$\rho(\phi) := \rho_2 + (\rho_1 - \rho_2)H(\phi) \quad \text{and} \quad \mu(\phi) := \mu_2 + (\mu_1 - \mu_2)H(\phi)$$

where $H(\phi)$ denotes the Heaviside function which is defined as

$$H(\phi) := \begin{cases} 0 & \text{if } \phi < 0 \\ \frac{1}{2} & \text{if } \phi = 0 \\ 1 & \text{if } \phi > 0. \end{cases}$$

Now, with these ϕ-dependent material parameters, equation (2.12) can be expressed as

$$\int_\Omega \rho(\phi)\frac{D\vec{u}}{Dt} \, d\vec{x} = \int_\Omega \nabla \cdot \mathbf{T} \, d\vec{x} - \int_{\Gamma_f} \sigma\kappa\vec{n} \, dF + \int_\Omega \rho(\phi)\vec{g} \, d\vec{x}. \tag{2.14}$$

Following Chang et al. [6] we now rewrite the free boundary integral as a volume integral with the help of a Dirac δ-functional. Since $\vec{n} = \frac{\nabla\phi}{|\nabla\phi|}$ and $|\nabla\phi| = 1$, this results in the identity

$$\int_{\Gamma_f} \sigma\kappa\vec{n} \, dF = \int_\Omega \sigma\kappa(\phi(\vec{x}))\delta(\phi(\vec{x}))\nabla\phi(\vec{x}) \, d\vec{x} \tag{2.15}$$

where δ denotes the one-dimensional Dirac δ-functional, i.e. $\int_\mathbb{R} f(x)\delta(x) \, dx = f(0)$ for $f : \mathbb{R} \to \mathbb{R}$, such that $\int_{\mathbb{R}^3} \delta(\phi(\vec{x})) \, d\vec{x} = \int_{\Gamma_f} 1 \, ds$. We substitute (2.15) into (2.14) and obtain

$$\int_\Omega \left(\rho(\phi)\frac{D\vec{u}}{Dt} - \nabla \cdot \mathbf{T} + \sigma\kappa(\phi)\delta(\phi)\nabla\phi - \rho(\phi)\vec{g} \right) d\vec{x} = 0$$

which now only involves a volume integral. Since this relation holds for any arbitrary volume Ω, we obtain the associated differential equation

$$\rho(\phi)\frac{D\vec{u}}{Dt} - \nabla \cdot \mathbf{T} + \sigma\kappa(\phi)\delta(\phi)\nabla\phi - \rho(\phi)\vec{g} = 0.$$

With the definition of the stress tensor $\mathbf{T} = -p\mathbf{I} + \mu(\phi)\mathbf{S}$, this yields the equation

$$\rho(\phi)\frac{D\vec{u}}{Dt} + \nabla p = \nabla \cdot (\mu(\phi)\mathbf{S}) - \sigma\kappa(\phi)\delta(\phi)\nabla\phi + \rho(\phi)\vec{g}. \tag{2.16}$$

In addition to (2.16) we need to take into account the continuity equation

$$\nabla \cdot u = 0, \tag{2.17}$$

and the time-dependence of the free-surface Γ_f. This time-dependent movement is modeled by a simple advection of the interface due to the underlying flow. Hence, we complement (2.16) and (2.17) by the simple transport equation

$$\partial_t\phi + \vec{u} \cdot \nabla\phi = 0 \tag{2.18}$$

for the level set function with initial value $\phi_0(\vec{x}) = \phi(\vec{x}, 0)$.

3. Numerical Method. In this section we present our overall numerical scheme for the treatment of the two-phase flow equations with surface tension in three space dimensions as given by (2.16), (2.17), and (2.18). The scheme is based on the well-known projection method. It employs a semi-implicit time-stepping scheme and a finite difference discretization in space on a staggered grid which is also used for the approximation of the level set function. We begin with a short review of the classical projection method before we cover the details of the incorporation of the level set method into the projection scheme. Here, we need to be concerned with three major issues: the movement of the interface and the conservation properties of the overall scheme, the discontinuity of the material properties at the interface, and the accurate approximation of the surface tension.

The movement of the free interface is modeled via the transport equation (2.18) for the level set function ϕ. Here, we have to deal with the problem of volume and mass conservation of the two different fluid phases. Hence, we employ a fifth order WENO scheme for the evaluation of all convective terms and reinitialize the level set function ϕ in every time-step to maintain the signed distance property of ϕ over time. Furthermore, we use an additional fixed point iteration to enforce the conservation of the global mass explicitly. Note that the discontinuity of the density and viscosity at the interface may lead to spurious oscillations and instabilities, therefore we need to be concerned with the development of an appropriate smoothing scheme for the material properties. Moreover, it is essential to employ a higher order interpolation scheme for the level set function to obtain an accurate approximation of the surface tension. In the following we cover these issues in some more detail.

3.1. Time Discretization and Projection Method. A widely used and very successful scheme for the solution of the incompressible Navier–Stokes equations is the so-called projection method due to Chorin [9]. Here, the starting point is the consideration of the time-discrete Navier–Stokes equations using a forward Euler scheme; i.e., we compute the solution $\vec{u}^{n+1}$ at time t_{n+1} from the solution $\vec{u}^n$ of the previous time step. To obtain the solution of (2.16) under the constraint (2.17) in a single Euler-step, we employ a two step approach. First, we compute an intermediate velocity field $\vec{u}^*$ via an explicit transport which may not yield $\vec{u}^*$ to be divergence free. Then, in a second step, we compute a correction ∇p^{n+1} of the intermediate velocity field $\vec{u}^*$ by the pressure Poisson equation which leads to a divergence free velocity field $\vec{u}^{n+1}$; i.e., we treat the pressure (and the level set function) implicitly.

By an Euler time-discretization of (2.16) we obtain the intermediate velocity field $\vec{u}^*$ as

$$\frac{\vec{u}^* - \vec{u}^n}{\delta t} = -(\vec{u}^n \cdot \nabla)\vec{u}^n + \vec{g} + \frac{1}{\rho(\phi^n)}\Big(\nabla \cdot (\mu(\phi^n)\mathbf{S}^n) - \sigma\kappa(\phi^n)\delta(\phi^n)\nabla\phi^n\Big) \qquad (3.1)$$

using the definition of the material derivative $\frac{D(\vec{u}_i)}{Dt} := \partial_t(\vec{u}_i) + (\vec{u}_i \cdot \nabla)\vec{u}_i$. The superscript n indicates the respective time step. With this definition, we can rewrite the time-discrete Navier–Stokes equations as

$$\frac{\vec{u}^{n+1} - \vec{u}^*}{\delta t} + \frac{\nabla p^{n+1}}{\rho(\phi^{n+1})} = 0, \qquad (3.2)$$

$$\nabla \cdot \vec{u}^{n+1} = 0. \qquad (3.3)$$

Note that the level set function ϕ^{n+1} at time step $n+1$ must be available for the definition of (3.2). To this end (2.18) must be solved for the $(n+1)$th time step prior to the treatment of (3.2), see the next section for the construction of ϕ^{n+1}.

Now, we apply the divergence operator to equation (3.2), multiply by -1, and with (3.3) we arrive at the pressure Poisson equation with the density field as diffusion coefficient

$$-\nabla \cdot \Big(\frac{1}{\rho(\phi^{n+1})}\nabla\hat{p}^{n+1}\Big) = -\nabla \cdot \vec{u}^* \qquad (3.4)$$

where $\hat{p}^{n+1} := \delta t p^{n+1}$. We obtain appropriate boundary conditions for the pressure Poisson equation by projecting the vector equation (3.2) onto the outer unit normal of the domain boundary

$$\frac{\partial p^{n+1}}{\partial \vec{n}}\Big|_{\Gamma} = \frac{\rho}{\delta t}(\vec{u}^*_{\Gamma} - \vec{u}^{n+1}_{\Gamma}) \cdot \vec{n}.$$

Thus, if we require $\vec{u}^{n+1}_{\Gamma} = \vec{u}^*_{\Gamma}$, we obtain homogeneous Neumann boundary conditions for the pressure

$$\frac{\partial \hat{p}^{n+1}}{\partial \vec{n}}\Big|_{\Gamma} = 0.$$

To ensure the existence of a solution, we also need to fulfill the compatibility condition

$$0 = \int_{\Omega} \nabla \cdot \vec{u} \, d\vec{x} = \int_{\Gamma} \vec{u} \cdot \vec{n} \, ds$$

which expresses the fact that the velocity on the boundary Γ must have a vanishing total flux. Note that the employed space discretization must comply with this requirement. Now, we can solve the system (3.4) for $\hat{p}^{n+1} = \delta t p^{n+1}$, at least up to a constant. We fix this remaining degree of freedom in the pressure p^{n+1} via the additional condition

$$\int_{\Omega} p^{n+1} \, d\vec{x} = 0$$

to ensure the comparability of the pressure results at different times t_n. Finally, we obtain a correction of the intermediate velocity field $\vec{u}^*$ such that the velocities at time t_{n+1}

$$\vec{u}^{n+1} = \vec{u}^* - \frac{1}{\rho(\phi^{n+1})}\nabla\hat{p}^{n+1} \qquad (3.5)$$

are now divergence free.

The extension of Chorin's projection method to higher order multi-step time-discretizations is straightforward. Throughout this paper we use a second order Adams–Bashford scheme for the integration of the momentum equation (3.1), i.e.

$$\frac{\vec{u}^* - \vec{u}^n}{\delta t_n} = \frac{1}{2}\left(\frac{\delta t_n + 2\delta t_{n-1}}{\delta t_{n-1}}L^n - \frac{\delta t_n}{\delta t_{n-1}}L^{n-1}\right) \tag{3.6}$$

where $\delta t_n = t_n - t_{n-1}$ denotes the length of the nth time step and L^n the right-hand side of (3.1) evaluated at time t_n.

3.2. Time Discretization and the Level Set Function. In the following we consider the time discretization of the transport equation (2.18) for the level set function ϕ and its effect on the signed distance property of ϕ. The discretization is based on a second order Adams–Bashford scheme (3.6) for time discretization and a fifth order WENO scheme [28,29] for the discretization of the convective term $\vec{u}^n \cdot \nabla \phi^n$. Furthermore, we use a third order Lagrange interpolation scheme for the evaluation of the velocities at the cell centers.

Note that in general the transport of the level set function ϕ due to (2.18) will destroy its signed distance property. This property however is essential for the stable approximation of surface tension. Hence, a transported level set function should not be used directly for the approximation of curvature or the surface tension. Instead, we refer to the transported level set function as an intermediate level set function ϕ^*; i.e., the time-stepping scheme gives ϕ^* and not ϕ^{n+1} so that

$$\phi^* = \phi^n + \frac{\delta t}{2}(3u^n \cdot \nabla\phi^n - u^{n-1} \cdot \nabla\phi^{n-1}) \tag{3.7}$$

To obtain a valid signed distance function ϕ^{n+1} from ϕ^* a reinitialization must be employed. There exist a number of variants for the reinitialization of the level set function, the one we employ in our implementation is essentially due to Sussman et al. [45]. Here, we give a short review of this scheme for the sake of completeness.

Consider a given function $\phi^*(\vec{x})$ whose zero-level set is the fluid interface. To generate the appropriate signed distance function $\phi^{n+1}(\vec{x})$ with an approximately identical zero-level set as $\phi^*(\vec{x})$, we discretize the following pseudo-transient Hamilton–Jacobi problem

$$\partial_\tau d + \text{sign}(\phi^*)(|\nabla d| - 1) = 0 \tag{3.8}$$

and evolve it to steady state with the initial value $d(\vec{x}, 0) = \phi^*(\vec{x})$. Note that the term $\text{sign}(\phi^*)|\nabla d|$ can be interpreted as motion along the normal direction away from the zero level set. Since our numerical approach relies on the signed distance property in the vicinity of the free surface only it is sufficient to compute the solution of (3.8) in an $\epsilon(\vec{x})$-neighborhood of the zero-level set. This is also the region where the largest deviation from the exact signed distance occurs due to the transport of the level set function. The parameter $\epsilon(\vec{x})$ must be chosen with respect to the spatial resolution of the employed numerical scheme, see the next section. The Hamilton-Jacobi reinitialization (3.8) is discretized using a third order TVD Runge–Kutta [43] method in time and a fifth order WENO scheme in space.

For the numerical treatment of (3.8) it is advisable to employ a regularized signum function since this leads to better conservation properties as well as a more stable
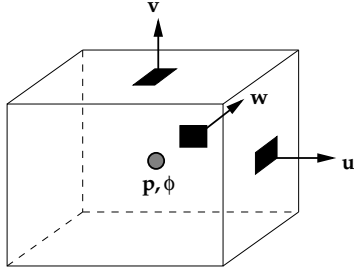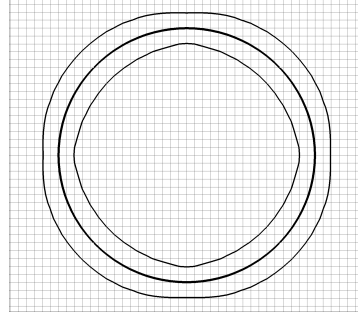
9

FIGURE 3.1. *Variables in a staggered grid.*

FIGURE 3.2. *Numerical smoothing region defined in* (3.14) *for the material parameters.*

approximation.[1] There exist various different regularization approaches, e.g. [40, 45]. In our implementation we employ the regularized signum function

$$\widetilde{\text{sign}}(\phi^*) = \frac{\phi^*}{\sqrt{(\phi^*)^2 + |\nabla \phi^*|^2 (\delta x^2)}}. \tag{3.9}$$

due to Peng et al. [40]. In the discrete setting the parameter δx is replaced by the spatial mesh-width h, see section 3.3. Since (3.9) takes the gradient of ϕ^* into account we obtain the discrete conservation of the sign of the level set function (in the grid nodes). Note that the smoothed signum function (3.9) needs to be updated before each Euler-substep in the Runge–Kutta scheme.

To further improve the conservation properties of our method we employ an additional Picard iteration

$$\phi^{n+1} \leftarrow \phi^{n+1} + \omega(V_1(\phi^0) - V_1(\phi^{n+1})) \tag{3.10}$$

where $V_1(\phi^0)$ denotes the initial volume of Ω_1^0 and $V_1(\phi^{n+1}) := \int_\Omega H(\phi^{n+1}) \, dx$ is the volume of Ω_1^{n+1} after the reinitialization step to enforce the conservation of mass globally over time.

3.3. Space Discretization. Let us now consider the numerical treatment of the momentum equation. To this end, we need to specify the spatial discretization scheme. Here, we employ a widely used finite difference/finite volume scheme on a staggered grid to discretize the velocity field $\vec{u} := (u, v, w)^T$ and the pressure p; i.e., the cell centers $x_{i,j,k}$ correspond to the pressure nodes whereas the cell-face centers $x_{i+\frac{1}{2},j,k}$, $x_{i,j+\frac{1}{2},k}$, and $x_{i,j,k+\frac{1}{2}}$ give the velocity nodes for u, v, and w, respectively, see e.g. [20]. Furthermore, we discretize the level set function ϕ in the pressure nodes, see Figure 3.1. Note that all discrete fields are denoted by a subscript h, e.g., the discrete velocity in x-direction is given by u_h and the discrete level set function by ϕ_h.

The computation of the discrete intermediate velocity $\vec{u}_h^*$ in (3.1) requires the discretization of the viscous terms $\nabla \cdot (\mu(\phi_h^n)\mathbf{S}_h^n)$ in the velocity nodes of the staggered grid. Since the velocities are continuous for viscous fluids (and due to the use of a

---

[1]Note that this regularization scheme is independent of the smoothing of the material parameters given in section 3.4 which is required for the treatment of surface tension effects only. However, we *always* use a regularized signum function.

smoothed viscosity, compare (3.11)) the first and second order derivatives are approximated with central differences. Note however that we need to employ an appropriate interpolation scheme to evaluate the discrete level set function ϕ_h in all velocity nodes, i.e. in the cell-face centers, since ϕ_h is itself given in the pressure nodes, i.e. in the cell centers. To this end, we use a third order Lagrange interpolation scheme.

To be able to treat convection dominated flow problems, it is essential to employ a higher order discretization for the convective terms. Here, we use a fifth order WENO scheme [28, 29] for the treatment of all convective terms, see [10] for details. This approach yields very good conservation properties even in the presence of large velocity gradients and allows for a stable approximation of the curvature. Note that an appropriate interpolation scheme for the velocities is required to apply the employed fifth order WENO scheme. Again, we use a third order Lagrange interpolation.[2]

3.4. Smoothing, Surface Tension, Surface Normals and Curvature. So far we have neglected the discontinuity of the density at the interface. Yet, a jump in the diffusion coefficient in (3.4) can have a substantial adverse effect on the stability and the accuracy of our numerical scheme. Hence, we need to develop an appropriate smoothing scheme for the material properties, so that the density and the viscosity are at least continuous across the interface. This smoothing scheme, however, should not affect the approximation properties globally. Another issue here is of course the discretization of the Dirac delta functional introduced by the CSF-approach.

To this end, let us consider the interface as having the thickness $\epsilon(\vec{x})$ which is proportional to the spatial mesh-width h, see Figure 3.2. Then, we replace the discrete density $\rho(\phi_h)$ and the discrete viscosity $\mu(\phi_h)$ by

$$\rho^\epsilon(\phi_h) = \rho_2 + (\rho_1 - \rho_2)H^\epsilon(\phi_h) \quad \text{and} \quad \mu^\epsilon(\phi_h) = \mu_2 + (\mu_1 - \mu_2)H^\epsilon(\phi_h) \qquad (3.11)$$

where H^ϵ denotes a smoothed Heaviside function

$$H^\epsilon(\phi_h(\vec{x})) := \begin{cases} 0 & \text{if} \quad \phi_h(\vec{x}) \quad < \quad -\epsilon(\vec{x}), \\ \frac{1}{2}(1 + \frac{\phi_h(\vec{x})}{\epsilon} + \frac{1}{\pi}\sin(\frac{\pi\phi_h(\vec{x})}{\epsilon(\vec{x})})) & \text{if} \quad |\phi_h(\vec{x})| \quad \leq \quad \epsilon(\vec{x}), \\ 1 & \text{if} \quad \phi_h(\vec{x}) \quad > \quad \epsilon(\vec{x}). \end{cases} \qquad (3.12)$$

The associated smoothed delta functional is given by the derivative of (3.12), i.e.

$$\delta^\epsilon(\phi_h(\vec{x})) := \partial_{\phi_h} H^\epsilon(\phi_h(\vec{x})) = \begin{cases} \frac{1}{2\epsilon(\vec{x})}(1 + \cos(\frac{\pi\phi_h(\vec{x})}{\epsilon(\vec{x})})) & \text{if } |\phi_h(\vec{x})| \leq \epsilon(\vec{x}) \\ 0 & \text{else.} \end{cases} \qquad (3.13)$$

According to [16] a space- and ϕ_h-dependent smoothing region must be employed to account for mesh-alignment effects. We employ the smoothing region $|\phi_h(\vec{x})| \leq \epsilon(\vec{x})$ with

$$\epsilon(\vec{x}) = \alpha(\vec{x})h, \quad \text{where} \quad \alpha(\vec{x}) := c\frac{\|\nabla\phi_h(\vec{x})\|_1}{\|\nabla\phi_h(\vec{x})\|_2} < C \qquad (3.14)$$

with $c = 1.5$ in our implementation.

The fundamental assumption for the above smoothing scheme is that the gradient of the level set function is constant in the $\epsilon(\vec{x})$-region; i.e., that the contours of ϕ_h

---

[2]At the boundary of the computational domain we use a right- or left-weighted Lagrange interpolation. Note that for the evaluation of this higher order interpolation scheme some velocity values first need to be interpolated in the cell-face centers. Here, we use a two-dimensional Lagrange interpolation of third order. Close to the boundary, we employ a bilinear interpolation.

in the $\epsilon(\vec{x})$-region are symmetric to the zero-level set. Due to the choice of a signed distance function in our implementation this assumption is automatically satisfied.

Note that we employ the smoothed Heaviside function in the approximation of the volumes $V_1(\phi^0)$ and $V_1(\phi^{n+1})$ in the iteration (3.10). The respective integrals $\int_\Omega H^\epsilon(\phi_h)\,dx$ are approximated by a simple midpoint integration rule.

The use of the smoothed delta functional (3.13) reduces the quality of the approximation locally within the smoothing region by one order. To this end, consider a function g and its approximation g_h with a pointwise approximation error $g - g_h$ of order $O(h^p)$. Then, the smoothed error $(g-g_h)\delta^\epsilon$ is of the order $O(h^p)O(\epsilon(\vec{x})^{-1}) \approx O(h^{p-1})$ since $\epsilon(\vec{x}) \approx h$.

Finally, we must consider the approximation of the surface tension for the overall discretization of the momentum equation (2.16). Recall that the surface tension force enters as a singular source term which we converted to a volume integral using a delta functional and the CSF-approach. Hence, the main ingredient in the approximation of the surface tension is the use of the smoothed delta functional $\delta^\epsilon(\phi_i)$ given in (3.13) with ϵ defined in (3.14). This leads to a volumetric approximation of the surface tension force with support in the ϵ-neighborhood of the free surface, i.e.,

$$\sigma \kappa \delta(\phi)\vec{n} \approx \sigma \kappa_h \delta^\epsilon(\phi_h)\vec{n}_h.$$

Recall that the discrete unit normal $\vec{n}_h$ on the interface is given by $\vec{n}_h := \frac{\nabla \phi_h}{|\nabla \phi_h|}$ and the discrete curvature in three dimensions is defined as $\kappa_h := \nabla \cdot \vec{n}_h$. Note that even though we employ a signed distance function, i.e., $|\nabla \phi_h| = 1$ in the ϵ-neighborhood of the free surface, we compute $\vec{n}_h$ by $\frac{\nabla \phi_h}{|\nabla \phi_h|}$ rather than just by $\nabla \phi_h$. Similarly, we compute the discrete curvature κ_h by $\nabla \cdot \vec{n}_h$ rather than by $\Delta \phi_h$. This procedure allows for a more stable approximation of the surface normals as well as the curvature at cusps. Note that all differential operators in these computations are approximated using central differences.

Now that the momentum equations are discretized, it remains to discretize the pressure Poisson equation

$$-\nabla \cdot \frac{1}{\rho^\epsilon(\phi_h^{n+1})} \nabla \hat{p}_h^{n+1} = -\nabla \cdot \vec{u}_h^* \tag{3.15}$$

where $\rho^\epsilon(\phi_h^{n+1})$ denotes the smoothed discrete density field (3.11) after the advection step (3.7), the reinitialization (3.8) and the fixed point iteration (3.10). Since the velocities of an viscous fluid flow are sufficiently smooth, we compute the right-hand side of (3.15) with central differences. The left-hand side of (3.15) is discretized with a standard seven-point-stencil in the cell centers where the smoothed density field is evaluated in the cell-face centers via an interpolated level set function. According to section 3.1, we complement the pressure equation with homogeneous Neumann boundary conditions and enforce a vanishing mean for the pressure $p^{n+1} = (\delta t)^{-1} \hat{p}^{n+1}$. For the iterative solution of the resulting semi-definite diffusion equation we employ our parallel algebraic multigrid solver solver [21].

3.5. Adaptive Time Step Control. Since we employ an explicit scheme for the velocities we have to deal with a time step restriction due to the CFL-condition for explicit schemes. The CFL-condition takes convection, viscosity, surface tension and gravity into account and enforces that the discrete information can evolve no further than one grid cell since the discrete difference equations consider only fluxes between adjacent cells.

With the definitions $u_{\max} := \max_{i,j,k} |u_{i+\frac{1}{2},j,k}|$, $\kappa_{\max} := \max_{i,j,k} |\kappa_{i,j,k}|$, and

$$V := \max\left\{\frac{\mu_1}{\rho_1}, \frac{\mu_2}{\rho_2}\right\}\left(\frac{2}{(\delta x)^2} + \frac{2}{(\delta y)^2} + \frac{2}{(\delta z)^2}\right)$$

the overall time step restriction for the u component of the velocity field can be expressed as

$$\delta t^u \leq 2\,C_u$$

where

$$C_u := \left(\left(\frac{u_{\max}}{\delta x} + V\right) + \sqrt{\left(\frac{u_{\max}}{\delta x} + V\right)^2 + \frac{4|g_1|}{\delta x} + \frac{8\,\kappa_{\max}\sigma}{\alpha(\rho_2 + \rho_1)(\delta x)^2}}\right)^{-1}.$$

The bounds for δt^v and δt^w associated with the velocities in y- and z-direction involving C_v and C_w respectively are defined in an analogous way. Hence, we first obtain an appropriate time step restriction $\delta t^{u/v/w} \leq 2\,C_{u/v/w}$ for each velocity component separately. The final time step restriction can then be computed easily as the minimum of these three scalar bounds. This yields the overall time step restriction

$$\delta t \leq 2\,\xi\,\min_\Omega(C_u, C_v, C_w)$$

with a safety factor $\xi \in (0,1]$. Throughout this paper, we employ this adaptive time step control using $\xi = 0.3$ in our computations.

4. Numerical Results. In this section we present the results of our numerical experiments in three space dimensions. First we investigate the order of convergence obtained for the approximation of the curvature by means of a diagonally transported unit sphere. In particular we analyze the effect of the level set reinitialization and the fixed point iteration on the convergence of the curvature and the mass conservation properties of our numerical scheme. Then we examine the global order of convergence of our overall numerical scheme for two-phase flow problems including surface tension on the basis of a rising bubble test problem. Finally, we consider the deformation of a liquid droplet due to a surrounding shear flow.

4.1. Mass Conservation and Convergence of Curvature. First, we investigate the convergence behavior of our numerical scheme with respect to mass and curvature considering the simple test-case of an advected unit sphere. Since the curvature of the unit sphere is known analytically, we can directly compare the approximated curvature with the exact solution.

To this end, we consider the domain $\Omega = [0,4]^3$ which we discretize by a sequence of uniformly refined equidistant grids. Furthermore, we employ periodic boundary conditions on $\partial\Omega$ and a stationary velocity field

$$u(x,y,z) = 1, \quad v(x,y,z) = 1, \quad w(x,y,z) = 0.$$

As initial condition for the level set function we use the analytic distance function

$$\phi(x,y,z) = 1 - \sqrt{(x-2)^2 + (y-2)^2 + (z-2)^2} \tag{4.1}$$

whose zero-level set is a sphere with radius $r = 1$ centered at $(2,2,2)$; i.e., we transport the sphere over time along the diagonal in the xy-plane.
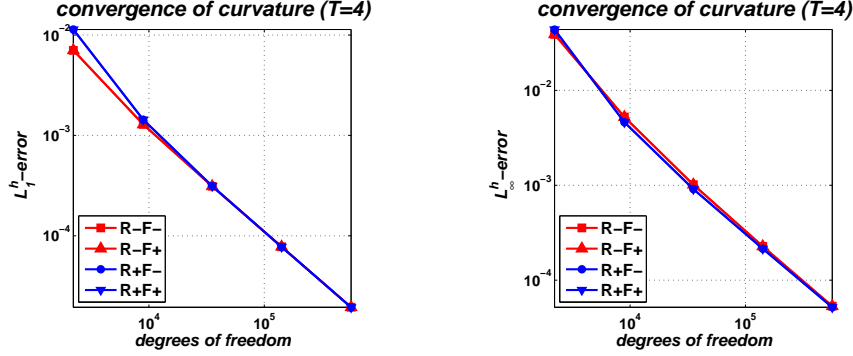
13

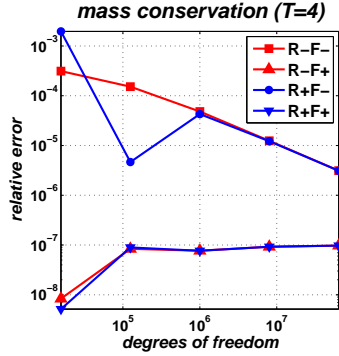FIGURE 4.1. *Convergence history for the curvature.*

FIGURE 4.2. *Convergence history for the relative error of mass.*

In this experiment we consider four different configurations of our numerical scheme to distinguish the effects on the convergence behavior associated with the reinitialization step and the fixed point iteration; i.e., we perform the simulation with/without reinitialization (3.8) and with/without fixed point iteration (3.10).

Recall that the curvature is defined as

$$\kappa_h(\phi_h)(\vec{x}) = \nabla \cdot \frac{\nabla \phi_h(\vec{x})}{\|\nabla \phi_h(\vec{x})\|}.$$

Let us furthermore define the following discrete error norms

$$e_\epsilon^{\kappa,h}(\vec{x}) := \frac{|\kappa_h(\phi_h)(\vec{x}) - \kappa_h(\phi)(\vec{x})|}{|\kappa_h(\phi)(\vec{x})|}, \tag{4.2}$$

$$e_{\epsilon,1}^{\kappa,h} := \sum_{\vec{x}_i, |\phi_h(\vec{x}_i)| < \alpha(\vec{x}_i)h} e_\epsilon^{\kappa,h}(\vec{x}_i), \tag{4.3}$$

$$e_{\epsilon,\infty}^{\kappa,h} := \max_{\vec{x}_i, |\phi_h(\vec{x}_i)| < \alpha(\vec{x}_i)h} e_\epsilon^{\kappa,h}(\vec{x}_i), \tag{4.4}$$

in the $\epsilon(\vec{x})$-region given by $|\phi_h(\vec{x}_i)| < \alpha(\vec{x}_i)h = \epsilon(\vec{x})$, compare 3.14. Thus, we measure the error not only on the interface but near the interface. Note that we do not employ the smoothed delta functional δ_ϵ in this computation. Recall that δ_ϵ is required only for the evaluation of surface tension force, it is not needed for the approximation of the curvature.

14

$1/h$	dof^h	dof_ϵ^h	$e_{\epsilon,1}^{\kappa,h}$	$\rho_{\epsilon,1}^{\kappa,h}$	$e_{\epsilon,\infty}^{\kappa,h}$	$\rho_{\epsilon,\infty}^{\kappa,h}$	$e_\epsilon^{m,h}$	$\rho_\epsilon^{m,h}$
			reinitialization $(-)$	fixed point $(-)$				
25	15625	2214	7.034_{-3}	$-$	3.890_{-2}	$-$	3.130_{-4}	$-$
50	125000	8928	1.288_{-3}	1.218	5.236_{-3}	1.438	1.521_{-4}	0.346
100	1000000	35376	3.119_{-4}	1.030	1.015_{-3}	1.192	4.823_{-5}	0.552
200	8000000	141440	7.773_{-5}	1.003	2.271_{-4}	1.080	1.244_{-5}	0.651
400	64000000	565768	1.943_{-5}	1.000	5.320_{-5}	1.047	3.123_{-6}	0.664
			reinitialization $(+)$	fixed point $(-)$				
25	15625	2214	1.133_{-2}	$-$	4.370_{-2}	$-$	1.969_{-3}	$-$
50	125000	8932	1.437_{-3}	1.481	4.622_{-3}	1.611	4.652_{-6}	2.909
100	1000000	35380	3.128_{-4}	1.108	9.112_{-4}	1.180	4.289_{-5}	-1.068
200	8000000	141440	7.769_{-5}	1.005	2.147_{-4}	1.043	1.220_{-5}	0.604
400	64000000	565768	1.943_{-5}	0.999	5.180_{-5}	1.026	3.105_{-6}	0.658
			reinitialization $(-)$	fixed point $(+)$				
25	15625	2214	7.034_{-3}	$-$	3.890_{-2}	$-$	8.338_{-9}	$-$
50	125000	8928	1.288_{-3}	1.218	5.236_{-3}	1.438	8.365_{-8}	-1.109
100	1000000	35376	3.120_{-4}	1.030	1.015_{-3}	1.192	7.702_{-8}	0.039
200	8000000	141436	7.773_{-5}	1.003	2.271_{-4}	1.080	9.244_{-8}	-0.087
400	64000000	565768	1.943_{-5}	1.000	5.320_{-5}	1.047	9.727_{-8}	-0.024
			reinitialization $(+)$	fixed point $(+)$				
25	15625	2214	1.131_{-2}	$-$	4.373_{-2}	$-$	5.157_{-9}	$-$
50	125000	8932	1.437_{-3}	1.479	4.623_{-3}	1.611	8.952_{-8}	-1.373
100	1000000	35380	3.129_{-4}	1.107	9.113_{-4}	1.180	7.659_{-8}	0.075
200	8000000	141436	7.769_{-5}	1.005	2.147_{-4}	1.043	9.238_{-8}	-0.090
400	64000000	565768	1.943_{-5}	0.999	5.180_{-5}	1.026	9.725_{-8}	-0.024

Furthermore, we measure the error with respect to the initial mass at time $t = 4$ via the discrete norms

$$m_\epsilon^{h,t} := \sum_{\vec{x}_i,\,|\phi_h(\vec{x}_i)|<\alpha(\vec{x}_i)h} H^\epsilon(\phi_h^t(\vec{x}_i))h^3 \;, \quad e_\epsilon^{m,h} := \frac{|m_\epsilon^{h,t} - m_\epsilon^{h,0}|}{|m_\epsilon^{h,0}|}. \qquad (4.5)$$

The respective algebraic convergence rates ρ are determined by

$$\rho := -\frac{\log \frac{e^{2h}}{e^h}}{\log \frac{\mathsf{dof}_{2h}}{\mathsf{dof}_h}} \qquad (4.6)$$

respectively.

Since we employ an absolute stopping criterion of 10^{-7} in the fixed point iteration we anticipate to find a constant error e_ϵ^m when the fixed point iteration is used independently of the reinitialization step. Due to the fact that we employ a constant velocity field in this experiment the signed distance property of the level set function is only slightly disturbed over time so that we anticipate to find very similar results for the cases with/without reinitialization.

The results of our numerical study are summarized in Table 4.1 and Figures 4.1 and 4.2. The convergence rates ρ_ϵ^m are obtained with respect to the total number of grid cells dof whereas the convergence rates ρ_ϵ^κ are determined with respect to the number of grid cells dof_ϵ in the $\epsilon(\vec{x})$-region. Since $\mathsf{dof}_\epsilon \approx h^{-2}$ the classical second order convergence corresponds to $\rho = 1$. Analogously we obtain classical second order convergence for the mass if $\rho = \frac{2}{3}$ since $\mathsf{dof} \approx h^{-3}$.

From the numbers displayed in Table 4.1 and the plots displayed in Figures 4.1 and 4.2 we can clearly observe this anticipated optimal convergence behavior of our
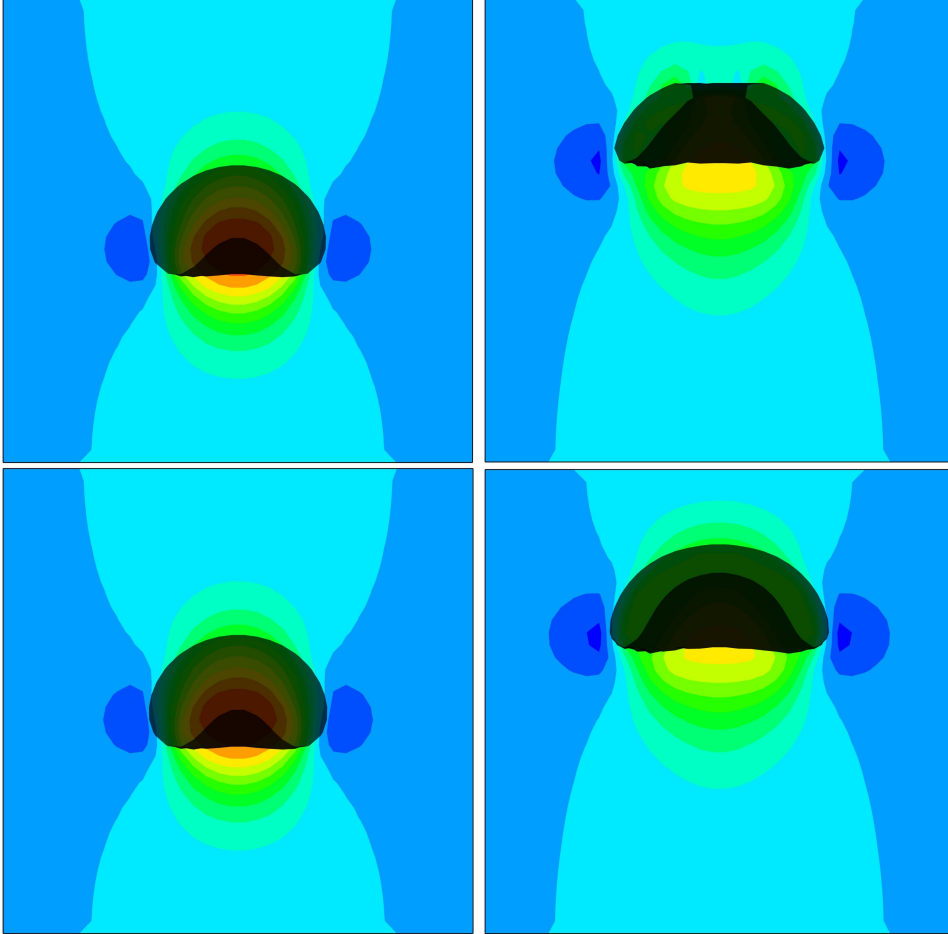
FIGURE 4.3. *Rising bubble without (upper row) and with (lower row) fixed point iteration for improved mass conservation at times $t = 0.075s$ (left column) and $t = 0.15s$ (right column) for $h = 1/37$. Depicted is a semi-transparent iso-surface of the zero-level set and a contour plot of the v-velocity along the center plane.*

TABLE 4.2
Parameter for rising bubble problem. Fluid$_1$ denotes the bubble and fluid$_2$ the surrounding fluid.

fluid$_1$:	$\mu_1 = 2.5_{-4}kg/ms$, $\rho_1 = 1.0_0 kg/m^3$	surface tension:	$\sigma = 5.0_{-3}N/m$
fluid$_2$:	$\mu_2 = 5.0_{-4}kg/ms$, $\rho_2 = 1.0_1 kg/m^3$	boundary conditions:	slip

numerical scheme. As expected the error with respect to mass is constant $< 10^{-7}$ if the fixed point iteration with absolute stopping criterion is used; i.e., we find the rate $\rho_\epsilon^m \approx 0$ due to the absolute stopping criterion. The reinitialization (R+) has almost no effect on the convergence behavior in this example since the distance property of the level set function is well-preserved over time due to the constant advection velocity.

4.2. Convergence for Two-Phase Flow with Surface Tension. To determine the convergence behavior of the complete two-phase flow solver including surface tension, we now consider a rising bubble reference problem. Here, a spherical bubble

Convergence study for rising bubble problem at time $t = 0.075s$.

$1/h$	$e_\infty^{u,h}$	$\rho_\infty^{u,h}$	$e_2^{u,h}$	$\rho_2^{u,h}$	$e_\infty^{v,h}$	$\rho_\infty^{v,h}$	$e_2^{v,h}$	$\rho_2^{v,h}$	$e_\infty^{w,h}$	$\rho_\infty^{w,h}$	$e_2^{w,h}$	$\rho_2^{w,h}$
					fixed point $(-)$							
37	3.92_{-1}	$-$	2.08_{-1}	$-$	1.13_{-1}	$-$	1.09_{-1}	$-$	3.92_{-1}	$-$	2.08_{-1}	$-$
73	2.09_{-1}	0.31	8.47_{-2}	0.44	7.67_{-2}	0.19	4.92_{-2}	0.39	2.09_{-1}	0.31	8.47_{-2}	0.44
145	6.94_{-2}	0.54	2.60_{-2}	0.57	3.52_{-2}	0.38	1.59_{-2}	0.55	6.94_{-2}	0.54	2.60_{-2}	0.57
					fixed point $(+)$							
37	3.87_{-1}	$-$	2.04_{-1}	$-$	1.20_{-1}	$-$	1.11_{-1}	$-$	3.87_{-1}	$-$	2.04_{-1}	$-$
73	2.06_{-1}	0.31	8.35_{-2}	0.44	6.96_{-2}	0.27	5.01_{-2}	0.39	2.06_{-1}	0.31	8.35_{-2}	0.44
145	6.76_{-2}	0.54	2.56_{-2}	0.57	2.97_{-2}	0.41	1.60_{-2}	0.56	6.76_{-2}	0.54	2.56_{-2}	0.57

Convergence study for rising bubble problem at time $t = 0.075s$.

$1/h$	$e_\epsilon^{m,h}$	$\rho_\epsilon^{m,h}$	$e_\infty^{\phi,h}$	$\rho_\infty^{\phi,h}$	$e_2^{\phi,h}$	$\rho_2^{\phi,h}$	$e_\infty^{p,h}$	$\rho_\infty^{p,h}$	$e_2^{p,h}$	$\rho_2^{p,h}$
					fixed point $(-)$					
37	4.621_{-2}	$-$	3.14_{-2}	$-$	1.89_{-2}	$-$	6.51_{-1}	$-$	1.14_{-2}	$-$
73	1.158_{-2}	0.679	1.27_{-2}	0.44	6.90_{-3}	0.50	5.89_{-1}	0.05	4.90_{-3}	0.41
145	2.402_{-3}	0.764	4.66_{-3}	0.49	2.19_{-3}	0.56	4.26_{-1}	0.16	1.92_{-3}	0.45
					fixed point $(+)$					
37	4.035_{-5}	$-$	3.49_{-2}	$-$	1.48_{-2}	$-$	6.52_{-1}	$-$	1.04_{-2}	$-$
73	2.343_{-5}	0.267	1.32_{-2}	0.48	6.32_{-3}	0.42	5.90_{-1}	0.05	4.55_{-3}	0.41
145	6.541_{-6}	0.620	4.46_{-3}	0.53	2.15_{-3}	0.52	4.27_{-1}	0.16	1.82_{-3}	0.45

of a lighter fluid rises and deforms in a denser fluid due to gravitational forces. The deformation behavior of the bubble is dominated by surface tension effects. Thus, we must consider surface tension forces in our numerical scheme so that the smoothed delta functional δ_ϵ is employed in these computations. Furthermore, the deformation of the spherical bubble is substantial over time so that a re-initialization step must be employed to enforce the signed distance property of the level set function for all times. To cope with the loss of mass due to the re-initialization of the level set function we again employ a global fixed point iteration. For comparison we also give the results obtained without the fixed point iteration.

We anticipate to find first order convergence near the free surface due to the smoothing of the delta functional whereas away from the free surface we expect to obtain a second order approximation since there, the smoothed delta functional is not active. Hence, we expect to find a global approximation order close to two.

The physical properties of the considered fluids are given in Table 4.2. The initial condition for the level set function ϕ corresponds to a spherical bubble with its center located at $(0.075m, 0.05m, 0.075m)$ and radius $r = 0.025m$. We consider the computational domain $\Omega = [0, 0.15m]^3$ which we discretize by three uniformly refined equidistant grids with mesh-width $h = 1/37, 1/73, 1/145$ together with the equidistant time steps $\delta t_h = 6.25_{-5}, 2.50_{-4}, 1.00_{-3}$, respectively.

Due to the lack of an analytical solution we employ a reference solution computed on a grid with mesh-width $1/289$ to assess the quality of our numerical scheme. To this end we make the definitions

$$E_h^{\mathrm{ref}}(\psi_h) := I_h^{\mathrm{ref}} \psi_h - \psi_{\mathrm{ref}},$$

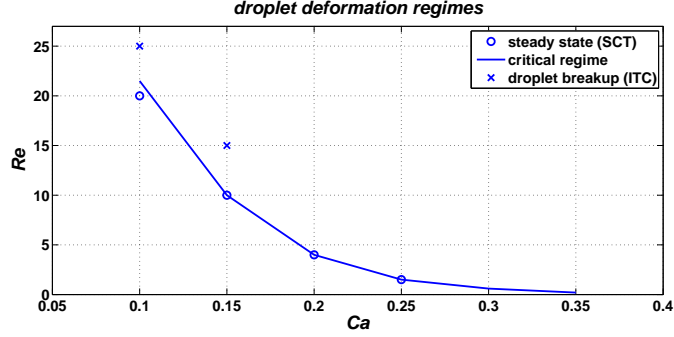where I_h^{ref} denotes a tri-linear interpolation of the data computed on a mesh with

FIGURE 4.4. *Phase diagram of droplet deformation with respect to the capillary number Ca and Reynolds number Re. The stationary regime with constant topology is indicated by SCT, the instationary regime where topological changes occur is indicated by ITC.*

mesh-width h to the reference mesh,

$$\|\psi_{\mathrm{ref}}\|_{L^2} := \frac{1}{N_{\mathrm{ref}}}\Big(\sum_{i=1}^{N_{\mathrm{ref}}} |\psi_{\mathrm{ref}}(\vec{x}_i)|^2\Big)^{1/2}, \quad \|\psi_{\mathrm{ref}}\|_{L^\infty} := \max_{i=1,\dots,N_{ref}} |\psi_{\mathrm{ref}}(\vec{x}_i)|,$$

and

$$e_{p,h}^{\psi} := \frac{\|E_h^{\mathrm{ref}}(\psi_h)\|_{L^p}}{\|\psi_{\mathrm{ref}}\|_{L^p}}. \tag{4.7}$$

We consider the convergence of the velocities u_h, v_h, w_h, the level set function ϕ_h, and the pressure p_h in this experiment. Again we determine the algebraic convergence rates according to (4.6) so that classical second order convergence is obtained if $\rho = \frac{2}{3}$. Since we must employ the smoothed delta functional to realize the surface tension in our simulation we cannot expect to find $\rho = \frac{2}{3}$ globally but we anticipate to find ρ between $\frac{1}{3}$ and $\frac{2}{3}$ only. On finer grids we expect to find ρ being closer to $\frac{2}{3}$ due to the smaller discrete surface to volume ratio; i.e., the smaller impact of the smoothing of the delta functional.

The measured relative errors (4.7) and the respective convergence rates (4.6) are given in Tables 4.3 and 4.4. From the displayed numbers we can observe the anticipated convergence behavior. We find convergence rates ρ between $\frac{1}{3}$ and $\frac{2}{3}$ approaching $\frac{2}{3}$ with decreasing mesh-width for the velocities with respect to the L^2-norm and the L^∞-norm. Furthermore, the results obtained for the u and w velocities are identical due to the symmetry of the problem. The relative errors and convergence rates attained for the level set function ϕ correspond very well to those of the velocities. Again we find ρ between $\frac{1}{3}$ and $\frac{2}{3}$ approaching $\frac{2}{3}$ on finer grids indicating a close to second order convergence also for the level set function. The positive effect of the fixed point iteration on the mass conservation is clearly visible from the measured relative errors $e_\epsilon^{m,h}$ given in Table 4.4. We obtain roughly five digits accuracy in mass with the fixed point iteration on all grids whereas without the fixed point iteration we find only up to three digits accuracy. The convergence behavior of the pressure p is as expected somewhat reduced due to the fact that the pressure is discontinuous across the interface.

4.3. Deformation of a Droplet in Shear Flow. Let us finally apply the presented numerical scheme to compute the deformation of a small droplet submitted
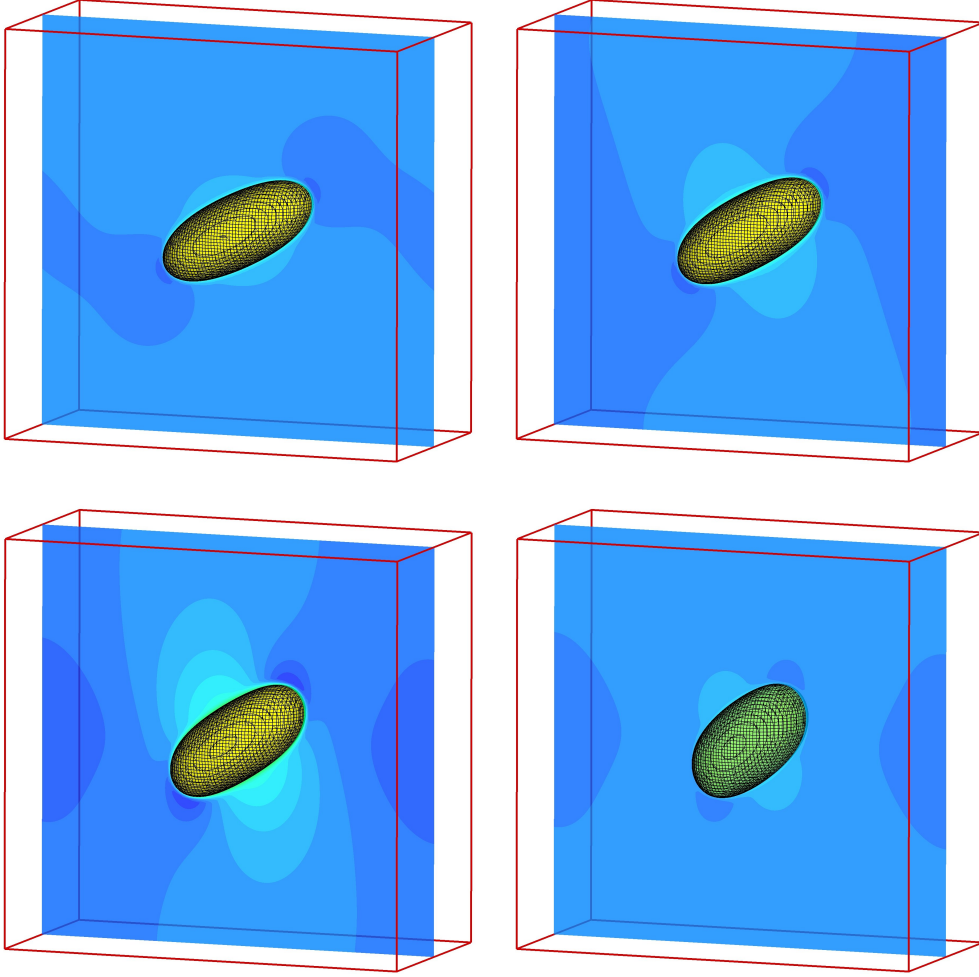
18

FIGURE 4.5. *Stationary results obtained for the four parameter settings* $(Ca, Re) = (0.25, 1.5)$, $(0.2, 4)$, $(0.15, 10)$, *and* $(0.1, 20)$ *(top left to bottom right). Depicted are the configuration of the free surface in the stationary limit. The respective pressure fields are color coded employing the same scaling in all plots. The stationary limits are reached at times* $t = 203.34$, $t = 538.41$, $t = 829.68$, *and* $t = 1649.36$ *(top to bottom). The simulation domain is* $2 \times 1 \times 2$ *and the droplet has a radius of* $r = 0.25$. *The mesh-width is* $(2/128, 1/64, 2/128)$.

to a shearing flow. To this end, we consider the idealized but representative reference problem of a circular drop with radius r_D sheared by a surrounding velocity field [4, 33, 34]. Here, the deformation behavior depends on the material properties of the two considered fluids and the employed shear rate $\dot{\gamma}$. For instance, we can obtain a steady state solution with a deformed (close to) elliptical droplet geometry in the case of sufficiently large surface tension force. On the other hand, if the surface tension force is too small to cope with the counteracting forces imposed by the shear flow, the droplet undergoes a change in topology and may be ruptured and breaks into daughter droplets [34].

Let us denote the viscosity of the surrounding fluid by ν_M and the viscosity of the droplet by ν_D. The characteristic non-dimensional parameter of such a problem
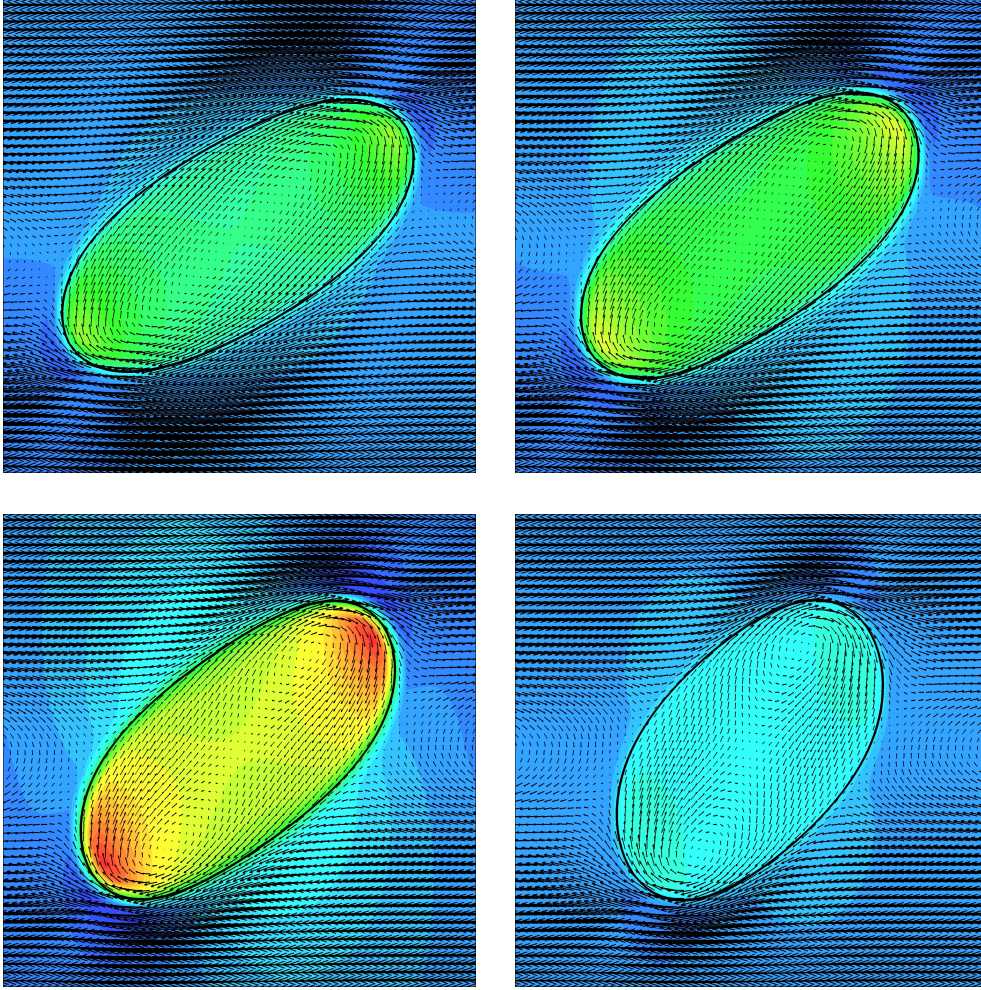
FIGURE 4.6. *Stationary results obtained for the four parameter settings $(Ca, Re) = (0.25, 1.5)$, $(0.2, 4)$, $(0.15, 10)$, and $(0.1, 20)$ (top left to bottom right). Depicted are zooms of the free surface in the surrounding flow field along the center plane (right). The respective pressure fields are color coded employing the same scaling in all plots. The stationary limits are reached at times $t = 203.34$, $t = 538.41$, $t = 829.68$, and $t = 1649.36$ (top to bottom). The simulation domain is $2 \times 1 \times 2$ and the droplet has a radius of $r = 0.25$. The mesh-width is $(2/128, 1/64, 2/128)$. For the parameters $(Ca, Re) = (0.25, 1.5)$, $(0.2, 4)$ (top row) the flow field inside the droplet has a single vortex, whereas for $(Ca, Re) = (0.15, 10)$, $(0.1, 20)$ (bottom row) we find two vortices.*

is the capillary number

$$Ca := \frac{\dot{\gamma} \nu_M r_D}{\sigma}. \tag{4.8}$$

The capillary number is a measure of the shear stress relative to the surface tension. The deformation behavior of the droplet is qualitatively determined by the capillary number Ca and the Reynolds number Re of the flow. According to [34] there are two flow regimes: A stationary regime (SCT) where the droplet attains its initial topology, and an instationary regime (ITC) where the droplet undergoes topological changes and is ruptured into daughter droplets over time, see Figure 4.4.
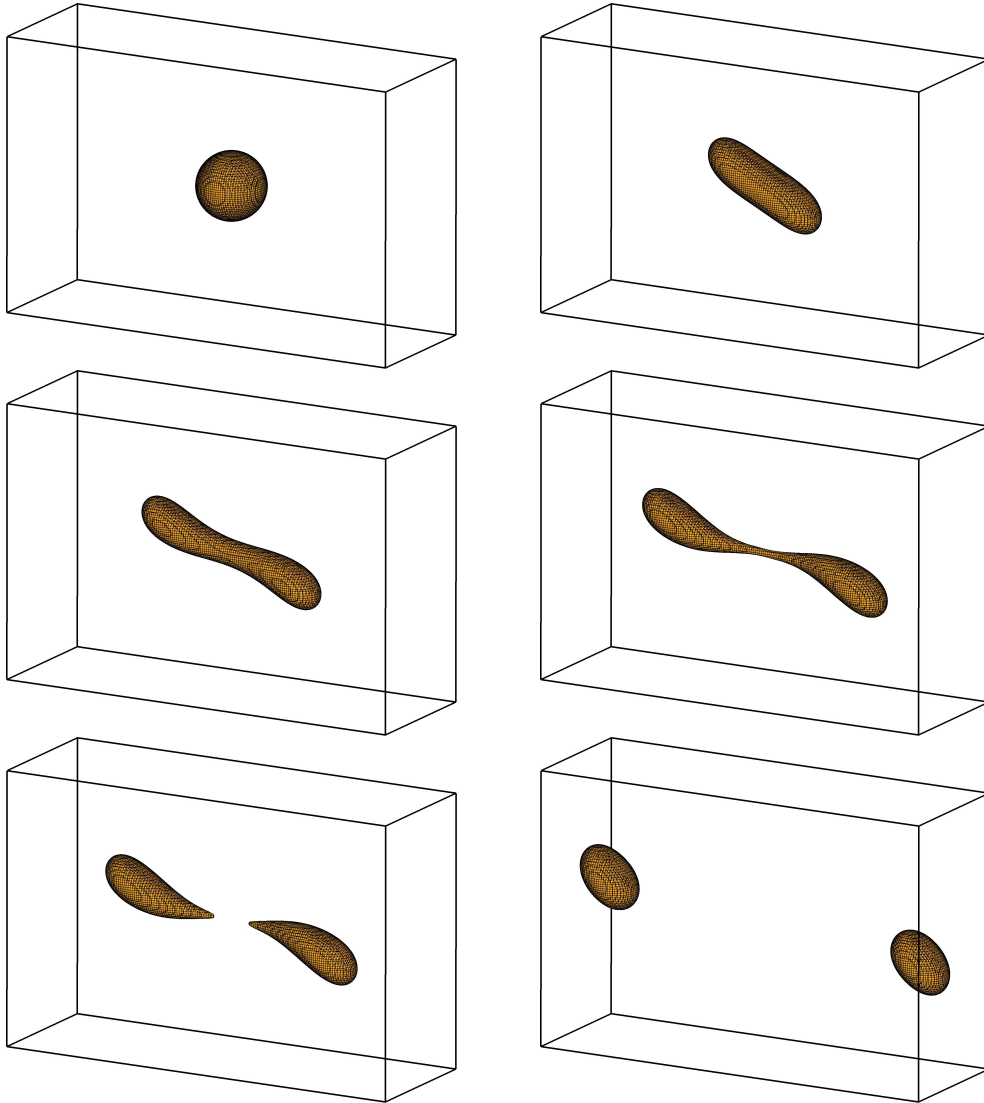
FIGURE 4.7. *Instationary results obtained for the parameter setting* $(Ca, Re) = (0.15, 15)$. *Depicted are the configuration of the free surface at the times* $t = 0$, $t = 334.8$, $t = 379.2$, $t = 396.0$, $t = 397.2$, $t = 416.40$ *(upper left to lower right). The simulation domain is* $3 \times 1 \times 2$ *and the droplet has a radius of* $r = 0.25$. *The mesh-width is* $(3/192, 1/64, 2/128)$.

First, we consider four representative parameter settings for the SCT-regime with Reynolds numbers just below the respective critical values, namely $(Ca, Re) = (0.25, 1.5)$, $(0.2, 4)$, $(0.15, 10)$, and $(0.1, 20)$. Note that these parameter choices were also considered in [33, 34] using a VOF-scheme. The final stationary results obtained for these settings are given in Figures 4.5 and 4.6. These results compare very well with those of [33, 34]. With increasing Reynolds number we also find a loss of symmetry of the droplet across the mid-plane and a stronger deviation of the droplet's geometry from an ellipsoidal shape. Furthermore, the flow field inside the droplet develops multiple vortices with increasing Reynolds numbers, e.g. we find just a single

FIGURE 4.8. *Instationary results obtained for the parameter setting* $(Ca, Re) = (0.1, 25)$. *Depicted are the configuration of the free surface at the times* $t = 0$, $t = 178.8$, $t = 238.8$, $t = 330.0$, $t = 358.8$, $t = 373.2$, $t = 394.8$, $t = 418.8$ *(top to bottom). The simulation domain is* $14 \times 1 \times 2$ *and the droplet has a radius of* $r = 0.25$. *The mesh-width is* $(14/896, 1/64, 2/128)$.

vortex for $(Ca, Re) = (0.25, 1.5)$ and $(Ca, Re) = (0.2, 4)$ and two vortices for the cases of $(Ca, Re) = (0.15, 10)$ and $(Ca, Re) = (0.1, 20)$.

Let us now consider several configurations from the instationary ITC regime. The results obtained for the parameter $(Ca, Re) = (0.15, 15)$ are given in Figure 4.7. Here, the droplet is stretched from spheroidal to ellipsoidal shape, then to a dumbbell shape before it is ruptured into two daughter droplets. These daughter droplets then converge to a steady state with respect to topology since surface tension is large

enough to prevent further break-up in this parameter setting.

For the parameters $(Ca, Re) = (0.1, 25)$ we anticipate to find a rupture of the droplet into more and smaller droplets over time since the balance of the surface tension and shear stress is valid up to large deformation. Thus, rupture occurs after this elongation phase for a strongly stretched dumbbell shaped droplet. Here, the ends pinch off and two rather large satellite droplets are spawned whose deformation behavior is similar to the initial droplet. The surrounding shear flow further elongates these three droplets and leads to further rupture of each of these droplets into smaller daughter droplets. This principal process continues until surface tension effects dominate the deformation behavior of the resulting daughter droplets; i.e., when the surface tension is larger than the shear stress. This anticipated behavior is clearly observable from the contour plots given in Figure 4.8.

5. Concluding remarks. In this paper we presented an incompressible Navier–Stokes solver for two-phase flow problems with surface tension in three dimensions. Our scheme employs a standard staggered grid finite difference discretization and a projection method with a fifth order WENO scheme.

The free surface between the two fluid phases is tracked with a level set approach. Here, the interface conditions are implicitly incorporated into the momentum equations by the CSF method and surface tension is evaluated using a smoothed delta functional and an appropriate third order interpolation scheme. Altogether, our approach exhibits a second order convergence away from the interface and a first order convergence near the interface if the smoothed delta functional is employed; i.e., in the presence of surface tension force. The results of our numerical experiments clearly show this anticipated convergence behavior. Furthermore, the presented results obtained for the deformation of a droplet in shear flow with moderate Reynolds numbers correspond very well to those obtained by VOF-schemes and the experimental data of [34].

REFERENCES

[1] D. ADALSTEINSSON AND J. A. SETHIAN, *A fast levelset method for propagating interfaces*, J. Comput. Phys., 118 (1995), pp. 269–277.

[2] A. AMSDEN AND F. HARLOW, *A simplified MAC technique for incompressible fluid flow calculations*, J. Comput. Phys., 6 (1970), p. 322.

[3] E. BÄNSCH, *Finite element discretization of the Navier–Stokes equations with a free capillary surface*, tech. rep., Universität Bremen, 1999.

[4] A. BÉLIVEAU, A. FORIN, AND Y. DEMAY, *A two-dimensional numerical method for the deformation of drops with surface tension*, Int. J. Comput. Fluid Dyn., 10 (1998), pp. 225–240.

[5] J. BRACKBILL, D. KOTHE, AND C. ZEMACH, *A continuum method for modeling surface tension*, J. Comput. Phys., 100 (1992), pp. 335–354.

[6] Y. CHANG, T. HOU, B. MERRIMAN, AND S. OSHER, *A level set formulation of Eulerian interface capturing methods for incompressible fluid flows*, J. Comput. Phys., 124 (1996), p. 449.

[7] S. CHEN, B. MERRIMAN, S. OSHER, AND P. SMEREKA, *A simple level set method for solving Stefan problems*, J. Comput. Phys., 135 (1997), pp. 8–29.

[8] D. L. CHOPP, *Computing minimal surfaces via level set curvature flow*, J. Comput. Phys., 106 (1993), pp. 77 – 91.

[9] A. CHORIN, *Numerical solution of the Navier–Stokes equations*, Math. Comput., 22 (1968), p. 745.

[10] R. Croce, M. Griebel, and M. A. Schweitzer, *A parallel level-set approach for two-phase flow problems with surface tension in three space dimensions*, Preprint 157, Sonderforschungsbereich 611, Universität Bonn, 2004.

[11] B. Daly, *Numerical study of two fluid Rayleigh–Taylor instability*, The Physics of Fluids, 10 (1967), p. 297.

[12] ———, *Numerical study of the effect of surface tension on interface instability*, The Physics of Fluids, 12 (1969), p. 1340.

[13] R. DeBar, *Fundamentals of the KRAKEN code*, report ucir-760, Lawrence Livermore National Laboratory, 1974.

[14] G. Dziuk, *Partial Differential Equations and Calculus of Variations*, vol. 1357, Springer, 1988, ch. Finite Elements for the Beltrami Operator on Arbitrary Surfaces, pp. 142–155.

[15] ———, *An algorithm for evolutionary surfaces*, Numer. Math., 58 (1991), pp. 603–611.

[16] B. Engqist, A.-K. Tornberg, and R. Tsai, *Discretization of dirac delte functions in level set methods*, J. Comput. Phys., 207 (2005), pp. 28–51.

[17] D. Enright, R. Fedkiw, J. Ferziger, and I. Mitchell, *A hybrid particle level set method for improved interface capturing*, J. Comput. Phys., 183 (2002), pp. 83–116.

[18] I. Ginzburg and G. Wittum, *Two-phase flows on interface refined grids modeled with VOF, staggered finite volumes, and spline interpolants*, J. Comput. Phys., (2001).

[19] I. Ginzburg, G. Wittum, and S. Zaleski, *Adaptive multigrid computations of multiphase flows*, in Numerical Flow Simulation III, E. Hirschel, ed., vol. 82 of Notes on Numerical Fluid Mechanics and Multidisciplinary Design, Springer, 2002, pp. 77–96.

[20] M. Griebel, T. Dornseifer, and T. Neunhoeffer, *Numerical Simulation in Fluid Dynamics, A Practical Introduction*, SIAM, Philadelphia, 1998.

[21] M. Griebel, B. Metsch, D. Oeltz, and M. A. Schweitzer, *Coarse grid classification: A parallel coarsening scheme for algebraic multigrid methods*, Numerical Linear Algebra with Applications, 13 (2006), pp. 193–214.

[22] M. Griebel, T. Neunhoeffer, and H. Regler, *Algebraic multigrid methods for the solution of the Navier–Stokes equations in complicated domains*, Int. J. Numer. Methods for Heat and Fluid Flow, 26 (1998), pp. 281–301.

[23] D. Gueyffier, J. Li, A. Nadim, R. Scardovelli, and S. Zaleski, *Volume-of-fluid interface tracking with smoothed surface stress methods for three-dimensional flows*, J. Comput. Phys., 152 (1999), pp. 423–456.

[24] F. Harlow and J. Welch, *Numerical calculation of time-dependent viscous incompressible flow of fluid with free surface*, The Physics of Fluids, 8 (1965), p. 2182.

[25] C. Hirt and B. Nichols, *Volume of fluid VOF method for the dynamics of free boundaries*, J. Comput. Phys., (1981), p. 201.

[26] L. Ho and A. Patera, *A Legendre spectral element method for simulation of unsteady incompressible viscous free-surface flows*, Comput. Methods Appl. Mech. Eng., (1990), pp. 355–366.

[27] L. Ho and E. Rønquist, *Spectral element solution of steady incompressible viscous free-surface flows*, Finite Elements in Analysis and Design, 16 (1994), pp. 207–227.

[28] G. Jiang and D. Peng, *Weighted ENO schemes for Hamilton–Jacobi equations*, SIAM J. Sci. Comput., 21 (2000), pp. 2126–2143.

[29] G. Jiang and C. Shu, *Efficient implementation of weighted ENO schemes*, J. Comput. Phys., 126 (1996), p. 202.

[30] B. Lafaurie, C. Nardone, R. Scardovelli, S. Zaleski, and G. Zanetti, *Modelling merging and fragmentation in multiphase flows with SURFER*, J. Comput. Phys., 113 (1994), p. 134.

[31] L. Landau and E. Lifshitz, *Fluid Mechanics*, Pergamon Press, Oxford, 1959.

[32] A. Lefebvre, *Atomization and Sprays*, Taylor & Francis, 1989.

[33] J. Li and Y. Y. Renardy, *Numerical study of flows of two immiscible liquids at low reynolds number*, SIAM Review, 42 (2000), pp. 417–439.

[34] J. Li, Y. Y. Renardy, and M. Renardy, *Numerical simulation of breakup of a viscous drop in simple shear flow through a volume-of-fluid method*, Phys. Fluids, 12 (2000), pp. 269–282.

[35] B. Merriman, J. Bence, and S. Osher, *Motion of multiple junctions: A level set approach*, J. Comput. Phys., 122 (1994), pp. 334–363.

[36] T. Neunhoeffer, *Numerische Simulation von Erstarrungsprozessen unterkühlter Flüssigkeiten unter Berücksichtigung von Dichteunterschieden*, Dissertation, Fakultät für Informatik der Technischen Universität München, 1997.

[37] W. Noh and P. Woodward, *SLIC–Simple line interface calculation*, in Fifth International Conference on Fluid Dynamics, Lecture Notes in Physics, A. V. Vooren and P. Zandbergen, eds., vol. 59, Springer, 1976, p. 330.

[38] S. Osher and R. Fedkiw, *Level Set Methods and Dynamic Implicit Surfaces*, no. 153 in Applied Mathematical Sciences, Springer, New York/Berlin/Heidelberg, 2003.

[39] S. Osher and J. Sethian, *Fronts propagating with curvature–dependent speed: Algorithms based on Hamilton–Jacobi formulations*, J. Comput. Phys., 79 (1988), pp. 12–49.

[40] D. Peng, B. Merriman, S. Osher, H. Zhao, and M. Kang, *A PDE-based fast local level set method*, J. Comput. Phys., 155 (1999), pp. 410–438.

[41] G. Russo and P. Smereka, *A remark on computing distance functions*, J. Comput. Phys., 163 (2003), pp. 51–67.

[42] J. A. Sethian, *Level Set Methods and Fast Marching Methods*, Cambridge University Press, 1999.

[43] C. Shu and S. Osher, *Efficient implementation of essentially non–oscillatory shock–capturing schemes*, J. Comput. Phys., 77 (1988), pp. 439–471.

[44] M. Sussman and E. Fatemi, *An efficient, interface preserving level set re-distancing algorithm and its application to interfacial incompressible fluid flow*, SIAM J. Sci. Comput., 20 (1999), p. 1165.

[45] M. Sussman, P. Smereka, and S. Osher, *A level set approach for computing solutions to incompressible two–phase flow*, J. Comput. Phys., 114 (1994), pp. 146–159.

[46] G. Tryggvason, B. Bunner, A. Esmaeeli, D. Juric, N. Al-Rawahi, W. Tauber, J. Han, S. Nas, and Y. Jan, *A front tracking method for the computations of multiphase flow*, J. Comput. Phys., 169 (2001), p. 708.

[47] S. Unverdi and G. Tryggvason, *A front-tracking method for viscous, incompressible multi-fluids flow*, J. Comput. Phys., 100 (1992), pp. 25–37.